Electrochimica Acta 513 (2025) 145450

Contents lists available at ScienceDirect

Electrochimica Acta

journal homepage: www.journals.elsevier.com/electrochimica-acta

pH dependence of noble metals dissolution: Iridium

Matej Zlatar [a,b,*], Daniel Escalera-López [a,1], Cornelius Simon [b], Valentín Briega-Martos [a], Kevin Stojanovski [a,b], Serhiy Cherevko [a,*]

[a] Forschungszentrum Jülich GmbH, Helmholtz-Institute Erlangen-Nürnberg for Renewable Energy (IET-2), Cauerstr. 1, 91058 Erlangen, Germany
[b] Department of Chemical and Biological Engineering, Friedrich-Alexander-Universität Erlangen-Nürnberg, Egerlandstr. 3, 91058 Erlangen, Germany

ARTICLE INFO

Keywords:
Iridium
Dissolution
Stability
pH
Phosphates
Buffer
OER

ABSTRACT

Iridium's stability and catalytic properties make it indispensable in a wide range of electrochemical applications including water electrolysis, yet its dissolution behavior across varying pH conditions remains poorly understood. This study addresses this gap by employing online inductively coupled plasma mass spectrometry (ICP-MS) to monitor iridium dissolution across a pH range of 1 to 12.7 under both pre-OER and OER conditions. An electrochemical protocol consisting of potential scans and holds is designed to track how potential and time affect Ir dissolution. In the pre-OER region, iridium shows consistent qualitative dissolution behavior across pH levels, although the extent of anodic and cathodic dissolution depends on the electrolyte. To explain this dependence, the thermodynamics of Ir in aqueous media, as revealed by the Pourbaix diagram, electrochemical profiles representing oxidation / reduction processes, and adsorption of electrolyte species are considered. During potential scans, kinetic effects from native oxides and phosphate adsorption lead to the absence of anodic dissolution, while prolonged holds at higher pH result in increased anodic dissolution, likely due to IrO_4^{2-} formation. Iridium's cathodic dissolution is observed in all studied protocols. It decreases from acidic to neutral pH, in line with the stability window of Ir^{3+} ionic species in the Pourbaix diagram, and surprisingly increases in highly alkaline conditions again, suggesting the existence of species not reflected on the diagram. In the OER region, iridium remains stable in acidic to neutral conditions, with stability decreasing under alkaline conditions. Two distinct dissolution mechanisms are proposed based on pH: in acidic environments, H_2O primarily acts as the reactant, leading to Ir^{3+} formation, while above pH 9, OH^- becomes the main reactant, contributing to IrO_4^{2-} formation and reduced stability. Under neutral conditions, buffers play a key role in maintaining local pH and supporting consistent OER rates, especially when the buffer's pK_a aligns with the solution's pH. These findings improve our understanding of iridium dissolution mechanisms and support the development of more stable and cost-effective iridium-based catalysts for various electrochemical technologies.

1. Introduction

The global drive towards net-zero emissions by 2050 reinforces the demand for renewable energy sources and associated technologies [1], particularly proton exchange membrane water electrolyzers (PEMWE). Within PEMWE systems, iridium-based catalysts are crucial for efficient catalysis of the otherwise sluggish oxygen evolution reaction (OER) at the anode. This is largely attributable to optimal binding energy of iridium with O*, OH*, and OOH* species [2,3], along with its exceptional stability under harsh acidic conditions and high anodic potentials [4]. This capability is crucial, as the OER is not only a key component of water electrolysis but also drives advancements across a wide array of energy conversion technologies.

On the other hand, limited availability and constraints in global supply chain of iridium hinder the worldwide scalability of PEMWE [5,6]. Another, often overlooked challenge is freshwater scarcity, projected to become increasingly critical at gigawatt and terawatt scales [7]. To address the challenges associated with iridium's limited availability and freshwater scarcity, innovative solutions are being explored. These include reducing iridium loading while improving its OER activity and stability [8], as well as pursuing alternative approaches such as seawater electrolysis with iridium catalysts [9,10]. Additionally, efforts are focused on recycling [11] and developing cost-effective iridium catalysts combined with less expensive metals [12].

* Corresponding authors.
E-mail addresses: m.zlatar@fz-juelich.de (M. Zlatar), s.cherevko@fz-juelich.de (S. Cherevko).
[1] Present address: Department of Interface Science, Fritz-Haber Institute of the Max-Planck Society, 14195 Berlin, Germany.

https://doi.org/10.1016/j.electacta.2024.145450
Received 30 August 2024; Received in revised form 18 November 2024; Accepted 1 December 2024
Available online 4 December 2024

To improve iridium stability in acidic environments, comprehensive understanding across different pH conditions is necessary. Previous studies have primarily focused on iridium stability in acidic [4,13,14] or alkaline [15] (where iridium often serves as a benchmark within the alkaline OER community [16,17]) environments, with some study exploring both conditions [18–20]. While iridium's stability tends to decrease in alkaline media, it has been shown to improve in mildly acidic conditions compared to strongly acidic environments [21]. These findings challenge earlier assumptions regarding pH in PEMWE and provide explanation for the catalyst stability discrepancies observed between model systems and membrane electrode assemblies (MEAs) [22].

Despite its relevance for applications such as anion exchange membrane (AEM) separated zero-gap CO_2 electrolyzer cells [23], iridium's performance in neutral or mildly acidic conditions remains largely unexplored. In these systems, iridium is often preferred over nickel at the anode, as the anolyte transitions from highly alkaline to near-neutral pH due to carbonate ion transport from the cathode [24]. This challenges the assumption that iridium's effectiveness is restricted to extreme pH conditions, suggesting its potential application across a broader pH range.

To reduce iridium loading, an understanding of the OER mechanism's is also important [25]. The kinetics of the OER process are inherently complex, as both H_2O and OH^- can serve as reactants [26]. This complexity is compounded by changes in reaction mechanisms, rate-determining steps, and alterations in the electrocatalyst surface state. The latter is influenced by its acid / base properties, determined by the nature of the metal oxide involved [26]. Gaining insights into OER reaction rate and pathway is achievable by investigating its pH dependence across a wide spectrum [25,27], as pH can significantly impact various parameters, including coupling between protons and electrons [25,28], charge density at the electrode, adsorption energies of intermediates, and stability of surface phases [29].

In addition, identifying the dominant OER mechanism across different pH values presents a significant challenge. A key factor contributing to this is the dynamic change in local pH near the electrode, occurring due to the consumption or production of H^+ or OH^- ions at the solid-liquid interface. This local pH can often differ significantly from the bulk solution's pH [30], as previously also demonstrated by Katsounaros et al., reporting that even a moderate reaction rate of merely 25 μA can cause substantial shifts in local pH, especially in electrolyte lacking buffering species [27,31]. Additionally, studies in both acidic [32] and alkaline [33] conditions have shown significant influences of electrolyte composition on OER activity.

Although some researchers caution against the use of buffers, others advocate for their use to stabilize pH, allow for accurate assessments of catalyst behavior, and better understand the reaction mechanism. Specifically, some argue that buffers may lead to potential poisoning, cation / anion effects, and introduce their own acid-base equilibria, all of which could obscure the true intrinsic activity of the catalyst and studies of OER mechanisms [25]. Moreover, even the addition of salts to maintain ionic strength is discouraged, as their presumed inertness may not be consistently reliable [34,35]. To avoid these issues, it was proposed to focus on pH ranges between 0 - 1.5 and 12.5 - 14, relying on water's inherent buffering capacity, thus eliminating the need for additional pH-stabilizing additives [25]. However, this methodology restricts the exploration of OER across a broader pH spectrum, where a detailed mechanistic understanding is still lacking [36,37].

When considering buffered media for OER studies to understand pH effects, it's important to note that buffers introduce additional ions like phosphates, acetates, or borates. These ions can adsorb onto the iridium surface [38–40], similar to platinum [41–44], thereby altering its electrochemical properties. Despite these potential drawbacks, this approach is still useful in understanding reaction mechanisms, is not unique to OER, and has been applied in various other reaction studies [29,45–49]. Buffers, when used strategically, enable a detailed study of the interactions that affect catalyst behavior under varied pH conditions [50–58].

In addition to understanding OER mechanisms and stability considerations discussed, the wide-ranging applications of iridium across advanced electrochemical systems emphasize the importance of studying its behavior under varied pH conditions. Beyond its foundational role in OER, iridium-based catalysts are essential for improving performances in a wide range of electrochemical devices that operate under extreme conditions. In the fuel cells, for example, iridium serves as an anode co-catalyst, significantly mitigating cell reversal damage during critical startup and shutdown phases. By facilitating OER over the carbon oxidation reaction (COR), iridium helps preserve carbon supports and platinum catalysts, effectively extending the operation lifetime of the fuel cell [59].

Iridium further demonstrates its versatility in solar water splitting applications, improving performance through the introduction of IrO_2 nanoparticles [60] or molecular catalysts [61–63] to electrode surface. This strategy improves charge transfer and minimizes recombination rates, directly addressing inherently slow kinetics of water oxidation and effectively reducing the photocurrent onset potentials. Additionally, when used as a protective overlayer, iridium enhances stability of electrode materials against photodegradation and introduces extra active sites for the reaction [64].

Additionally, in unitized regenerative fuel cells (URFCs), where developing a bifunctional electrocatalyst presents a critical challenge, iridium is combined with platinum to form a Pt / IrO_x catalyst. This catalyst efficiently catalyzes both the OER and the oxygen reduction reaction (ORR) under alternating operational modes [65]. Yet, the ongoing studies into the durability of these catalysts under operational conditions remains an active area of research [66,67].

Iridium's broad range of applications demonstrates its importance beyond traditional uses, especially in energy storage, medical devices, environmental sensing, and advanced display technologies. Its exceptional capacitive behavior and charge storage is harnessed in supercapacitors [68] and batteries [69,70], while its biocompatibility is crucial for durable and high-capacity neural stimulation electrodes [71]. In pH sensing applications, iridium microelectrodes excel, offering a wide response range, high sensitivity and stability, ensuring accurate and reliable measurements [72–75]. Additionally, its superior chemical stability offers significant advantages in electrochromic displays over traditional materials like nickel oxide, even though its less color-intensive [9,76]. Therefore, understanding iridium's stability across various pH conditions and at lower potential ranges compared to OER is important, as electrolyte pH can significantly affect the performance and durability of iridium catalysts. For examples, electrodes used in biosensing and environmental monitoring often encounter neutral to slightly alkaline electrolytes [77,78], while organic electrosynthesis demands catalysts that can withstand diverse solution conditions [79].

In summary, iridium stands as an important element in electrochemical systems, particularly for sustainable energy technologies. Its performance under varying pH conditions, its role in complex OER mechanisms, and the effects of electrolyte composition are key areas of study. However, emerging applications necessitate a detailed investigation of its stability across a wider pH spectrum, from acidic to basic conditions, and under both low and high potential operations. While Ir oxides are active materials in OER applications, reduction of IrO_x to metallic Ir may happen [80]. Therefore, understanding the stability of metallic Ir during oxidation / reduction is important as well. In some practical applications, we often rely on supporting electrolytes, hence studying iridium's stability during OER under such conditions is necessary, for example, in processes like CO_2 reduction reactions. These aspects are crucial in addressing the limited availability of iridium and leveraging its potential in developing efficient, less harsh, and sustainable electrocatalytic applications.

To address this, our study comprehensively investigated the influence of electrolyte composition and changes in OER mechanisms across

a broad pH range on iridium stability in buffered conditions, using phosphate buffer to prevent rapid local pH shifts that occur in unbuffered systems. Potential- and pH-dependent dissolution of polycrystalline iridium was measured directly by in-situ inductively coupled plasma mass spectrometry (ICP-MS) coupled with a scanning flow cell (SFC). This approach was further supported by a traditional rotating disk electrode (RDE) measurements using commercial iridium black catalyst. By systematically examining the effects of pH and potential on iridium dissolution, we aim to provide critical insights that improve the performance and durability of iridium-based systems across their full application spectrum. Additionally, this study contributes to optimizing existing electrocatalytic processes and opens avenues for novel iridium-based technologies in various scientific and industrial fields. It is part of a broader series exploring noble metal dissolution across wide pH range, which will include studies on gold [81], platinum [82], ruthenium and other metals.

2. Experimental section

2.1. Electrolyte preparation

In this study, a series of electrolytes were methodically prepared. A 0.05 M KOH solution (Sigma-Aldrich, 99.99 %) in ultrapure water (Merck, MilliQ®, 18.2 MΩ) was used as the electrolyte for pH 12.7. For the acidic pH 1 conditions, a 0.1 M $HClO_4$ elecrtrolyte was prepared by diluting 70 % $HClO_4$ (Suprapur, Merck) with ultrapure water. These conditions, although unbuffered, were still comparable to buffered environments as the concentration of OH^- and H^+ was sufficiently high, effectively compensating for pH fluctuations during the OER. For the specific preparation of a pH 1 electrolyte that included phosphates, we adjusted the concentrations of $HClO_4$ and H_3PO_4 (85 %, VWR) to 0.1 M and 0.05 M, respectively, ensuring that the final pH was accurately maintained at 1. Similarly, the pH 12.7 electrolyte with phosphate was prepared by adding 0.05 M H_3PO_4 to 0.1 M KOH. A borate buffer of pH 9 was prepared by diluting a 1.0 M $B(OH)_3$ (Sigma-Aldrich, 99.9 %) solution with water to achieve a final concentration of 0.05 M. The solution was then basified with 1.0 M KOH to reach the desired pH. Lastly, the unbuffered pH 3 electrolyte was prepared by dissolving $NaClO_4$ (Acros Organics, 99+%) in H_2O to a concentration of 0.05 M and acidified with $HClO_4$.

To prepare a range of intermediate pH values, we utilized 0.05 M phosphate-buffered electrolytes at pH 11, 9, 7, 5, and 3. These were diluted from a 1 M buffer solution of KH_2PO_4 / K_2HPO_4 (Merck, Suprapur®). For pH 11 and 3, we incrementally added 1 M KOH or 1 M $HClO_4$, respectively, until the target pH was achieved. The pH for each electrolyte was accurately measured using a (Mettler Toledo, FiveEasy Plus) pH meter immediately before conducting the experiments. Each electrolyte was freshly prepared before use to maintain consistency and reliability in our experimental setup.

2.2. Electrolyte pH determination and potential conversion

All the potentials in this study were converted to RHE scale using the conversion formula below:

$$E_{RHE} = E_{Ag/AgCl} + E^{0'}_{Ag/AgCl} + 0.059 \times pH$$

where $E_{Ag/AgCl}$ is measured potential and the $E^{0'}_{Ag/AgCl}$ is standard potential of the Ag / AgCl reference electrode.

The pH of each electrolyte was carefully determined. Initially, a buffer solution of KH_2PO_4 / K_2HPO_4 aimed at pH 7 was prepared, and its pH was accurately measured using a pH meter. The reliability of this measurement is particularly high as it falls within the mid-range of the pH meter's calibration curve. Afterwards, the open circuit potential (OCP) of a clean Pt wire, immersed in same solution (with precisely determined pH) saturated with H_2, was recorded against the Ag / AgCl reference electrode used in following experiments. This step established the exact potential for the reference electrode $E^{0'}_{Ag/AgCl}$. Prior to the SFC-ICP-MS measurements, the OCP of the Pt in the corresponding working electrolyte, also saturated with H_2, was determined. Using this data, the precise pH of the working electrolyte was calculated based on equation below, taking into account that the OCP for RHE is zero.

$$pH = \frac{-OCP_{Ag/AgCl} - E^{0'}_{Ag/AgCl}}{0.059}$$

2.3. In-situ activity / stability measurements using SFC-ICP-MS

All investigations regarding the in-situ electrochemical stability were carried out using a custom built polycarbonate Scanning Flow Cell (SFC) coupled with a NexION 350X (PerkinElmer) Inductively Coupled Plasma Mass Spectrometer (ICP-MS). The combination of electrochemistry and downstream analytics enabled real-time, in-situ detection of dissolved metal species during applied electrochemical protocols. The SFC was connected to a glassy carbon counter electrode (Sigma Aldrich, 99.995 % trace metals basis) and reference electrode (Metrohm, 3 M Ag / AgCl) using polymer tygon tubing (Proliquid), while polished iridium disk (MaTeck, Germany) used as a working electrode was approached from the top with an opening of the SFC, 0.011 cm^2.

The iridium disk was thoroughly polished using a polishing machine (Struers, LaboForce-100) and rinsed using isopropanol and ultra-pure water (18.2 MΩ, TOC < 5 ppb) before being positioned on the XYZ-translation stage (Physik Instrumente). The SFC setup was connected with a potentiostat (Gamry, Reference 600), controlled by custom LabVIEW software. This setup allowed precise control of potential, which was calibrated to the reversible hydrogen electrode (RHE) as detailed in section 2.2.

Electrolytes, prepared as outlined in the section 2.1, were first purged with argon and then pumped through the SFC at a regulated rate, monitored by the peristaltic pump of the ICP-MS. The flow rate of the electrolyte (~3.5 µL s^{-1}) was periodically calibrated, thereby ensuring a consistent supply to the ICP-MS.

A daily ICP-MS calibration and optimization was performed using solutions containing the different concentrations of iridium to generate 4-point calibration curve. ICP-MS sensitivity drifts were monitored by a simultaneous feed of internal standard with a similar mass and ionization potential (Re, 10 µg L^{-1}) as iridium. For detailed methodology and the specifics of the SFC-ICP-MS system, we direct readers to our previously published work [83,84], which provide further technical insights.

2.4. Offline activity / stability measurements using RDE

The ex-situ electrochemical activity / stability investigation was conducted using a rotating disk electrode (RDE) setup (Pine Research, USA), connected to a potentiostat (Biologic 150). The setup was coupled to a custom-built PTFE cell with a three-electrode configuration, consisting of an Ag / AgCl reference electrode submerged in a 3 M KCl solution, a graphite rod counter electrode, and a working electrode made from an Au disk (Ø ≈ 5 mm, Pine Research, USA) encased in PTFE to prevent any influence of backing electrode degradation on the obtained results [84]. Prior to each experiment, the Au disk, with a surface area of 0.1963 cm^2 was mirror-like polished using a 0.05 µm alumina suspension.

After polishing, the iridium thin film was prepared by drop-casting ink, following a method similar to that used for preparing ink for SFC-ICP-MS [13]. The ratio of H_2O to isopropanol was set at 3:1, and the weight ratio of catalyst (Ir Black, Alfa Aesar) to Nafion ionomer (5 wt.%, Sigma Aldrich) was adjusted to 2:1. To achieve a total iridium loading of approximately 32 µg cm^{-2}, 10 µL aliquots of 0.32 mg / mL ink were drop-cast twice, with a drying step in between, while rotating at 700 rpm. The electrolyte was prepared as outlined in the previous section and degassed for approximately 30 min via argon purging before the

beginning of each test. The procedure was conducted under a positive argon pressure, maintained in the RDE cell throughout the experiments. All potential values were corrected for iR by the electrolyte resistance obtained from the impedance spectroscopy measurement. Following the RDE protocol, 2 mL electrolyte aliquots were taken and analyzed by ICP-MS (offline mode) to determine Ir stability.

3. Results

To investigate Ir stability across a wide pH spectrum, we employed controlled pH conditions with a phosphate buffer (pH 3 – 11) and 0.1 M $HClO_4$ and 0.05 M KOH electrolytes for extreme pH environments at pH 1 and pH 12.7, respectively (Fig. 1a). A polished polycrystalline Ir disk served as the working electrode in SFC-ICP-MS analyses, with RDE measurements using Ir black on Au tips. Experimental protocols included potentiostatic holds and slow cyclic voltammetry (CV) with upper potential limits (UPL) of 1.2 and 1.6 V_{RHE} (Fig. 1b), with data normalized by electrochemical surface area (ECSA) to isolate trends in dissolution independent of surface area effects. For a detailed explanation of buffer choice, buffer concentration, buffering capacity, electrode selection, electrochemical protocol, and data normalization, see Sections S1-S2 in SI.

In Fig. 2, we present the CVs of polycrystalline Ir and Ir black obtained at the studied buffered electrolytes. For comparison, we also included the CVs of Ir wire measured in a bulk cell under static (no-flow) conditions, generally used in typical electrochemical setups as its preparation, such as flame annealing, is relatively simple [73–75, 85–88]. Notably, only the final CVs from a total of 20 cleaning cycles is shown, representing a stabilized surface. Moreover, the UPL was set to 1.2 V_{RHE}, in line with findings from our previous study which indicated that below this limit, the surface remains relatively stable, whereas above it, formation of hydrous oxide occurs [13]. CVs are in good agreement with those of metallic Ir and Ir black CVs previously reported in the literature [13,84,89,90] and reveal a good correlation between

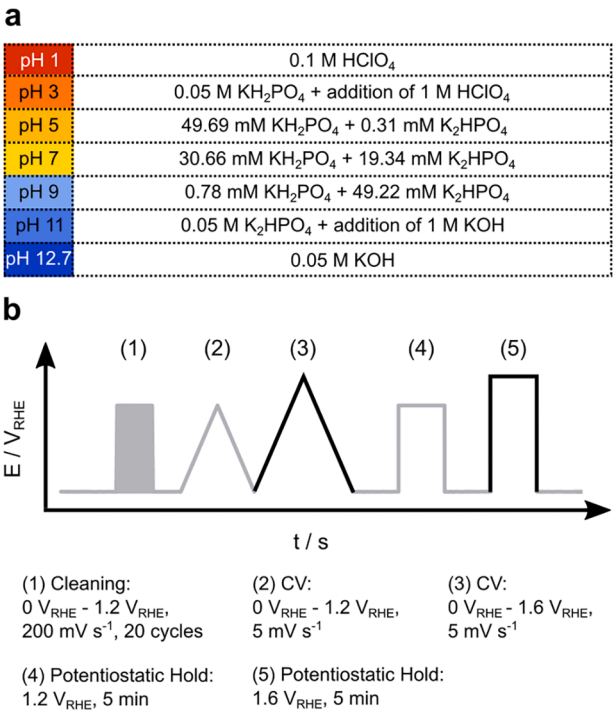

Fig. 1. Experimental details and protocol for pH-dependent activity-stability measurements. a) Variations in electrolyte composition and concentration across different pH values. b) Electrochemical protocol for SFC-ICP-MS, with highlighted parts focusing on the OER region.

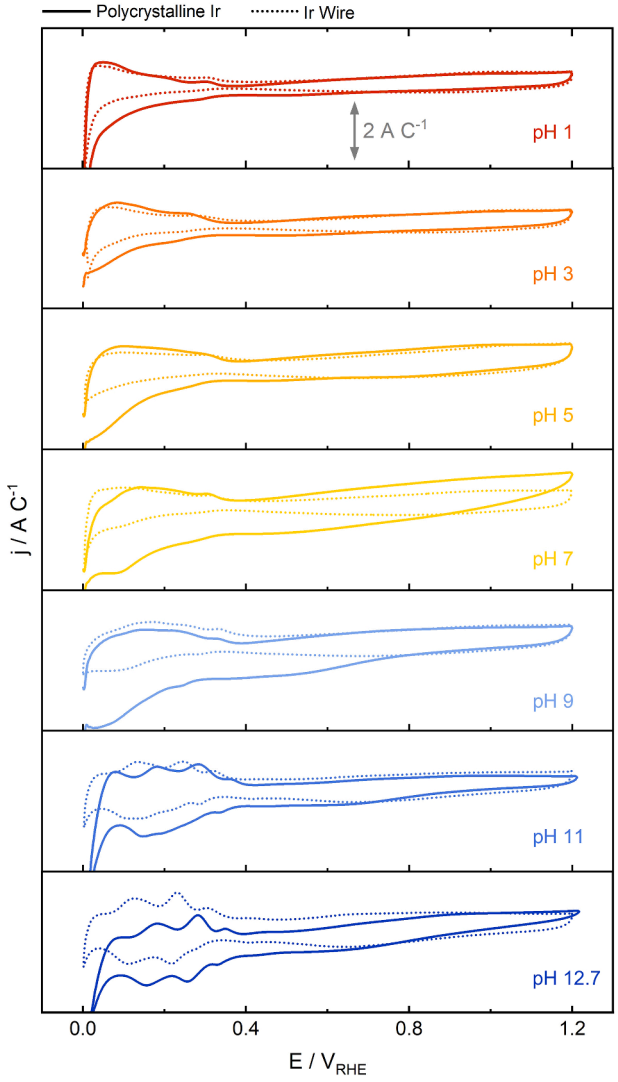

Fig. 2. Comparison of cyclic voltammograms for polycrystalline Ir (SFC) and Ir wire (bulk cell). Measurements were conducted in the 0 – 1.2 V_{RHE} range at a scan rate of 200 mV s^{-1}, showing the final cycle out of 20 total cycles.

the CVs of the polycrystalline Ir and Ir wire, affirming the validity of the results obtained via SFC-ICP-MS in this study. For further details on the CVs of Ir black and the pH-dependent shift of Ir^{III} / Ir^{IV} redox peaks, please refer to Section S3 in the SI.

3.1. pH- and Potential-Dependent dissolution profiles

Before we proceed with our analysis, it is important to acknowledge certain limitations when correlating Ir stability data from online ICP-MS to Pourbaix diagrams (Fig. 3 and S5). Originally, Pourbaix diagrams were constructed based on thermodynamic data under constant temperature and pressure, assuming infinite dilution and infinite time passed to reach equilibrium [15]. However, CV measurements involve non-equilibrium processes due to the continuously varying potential and relatively short time intervals. In such scenarios, kinetic effects such as reaction rates, mass transfer limitations, overpotentials, and concentration effects arise, which are not accounted for in the traditional Pourbaix diagrams [15,91]. Consequently, discrepancies may arise between the potential of phase transitions calculated from thermodynamics and those measured experimentally using online ICP-MS [15, 92]. Continuing on this discussion, it's important to also emphasize that thermodynamic data is valid for bulk states, while electrochemical

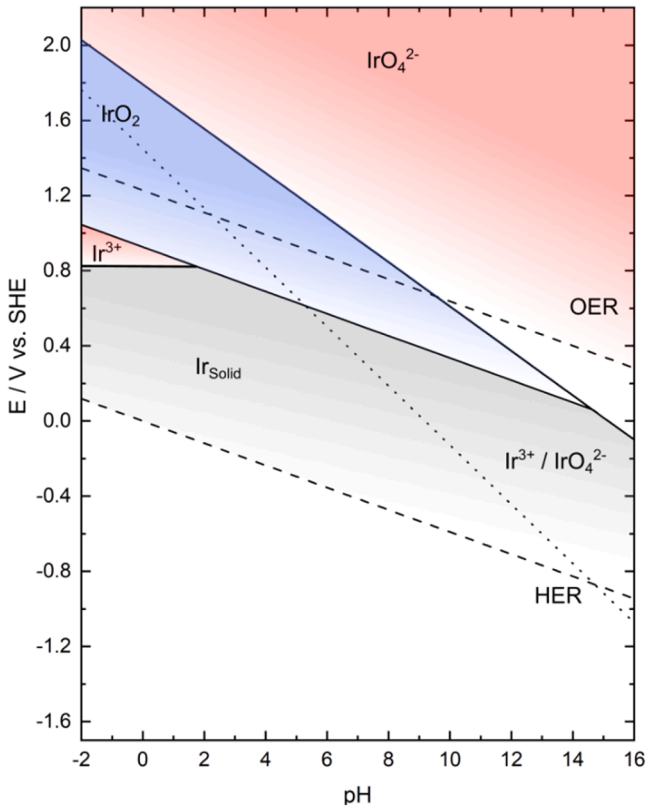

Fig. 3. Pourbaix diagram of iridium calculated with an equilibrium concentration of 1 nM.

reactions at the electrode's surface might have different reaction enthalpies or potentials [15,92].

We will frequently use the terms "anodic" and "cathodic" dissolution of iridium in the following results section. For a more detailed understanding of these processes, we encourage readers to refer to the studies by Cherevko et al. [4,13,14], and the discussion section of this work. Briefly, anodic dissolution of iridium occurs during oxidation, while cathodic dissolution follows the reduction of the formed oxide. The situation becomes more complex at an UPL of 1.6 V_{RHE}, where the OER occurs on the surface of iridium. Given that the OER mechanism and iridium dissolution share common intermediates [93], steady-state dissolution occurs, leading to continuous changes in the oxidation states of iridium [94].

Following Fig. 4 and Figure S6 presents the time-resolved, potential-dependent dissolution profiles of Ir as measured with an online ICP-MS setup. We evaluated Ir stability during slow-scan CV up to 1.2 and 1.6 V_{RHE} UPL, as seen in Fig. 4a, and during potentiostatic holds at the same potentials illustrated in Fig. 4b. CV represent potentiodynamic conditions in which Ir does not reach a thermodynamic equilibrium or a steady state due to the linear variation of potential over time. In contrast, the potentiostatic holds aim to represent a steady or quasi-steady state, serving as a point of comparison to the CV. The following dissolution profiles will be discussed with reference to the Pourbaix diagram (Fig. 3, S5 and S7) [91].

In Fig. 4a, within the pre-OER region, no anodic dissolution is observed during the slow potential scan up to an UPL of 1.2 V_{RHE}. However, in the following reverse scan, cathodic dissolution becomes apparent, showing a consistent decrease as pH increases. The dissolution trends observed during potentiostatic holds in Fig. 4b exhibit some differences compared to the observations during CV. When the potential is held for an extended time at 1.2 V_{RHE} (300 s, in contrast to the 0.2 s in CV), anodic dissolution is taking place and is more pronounced at alkaline pH values. Following the 1.2 V_{RHE} hold, cathodic dissolution at

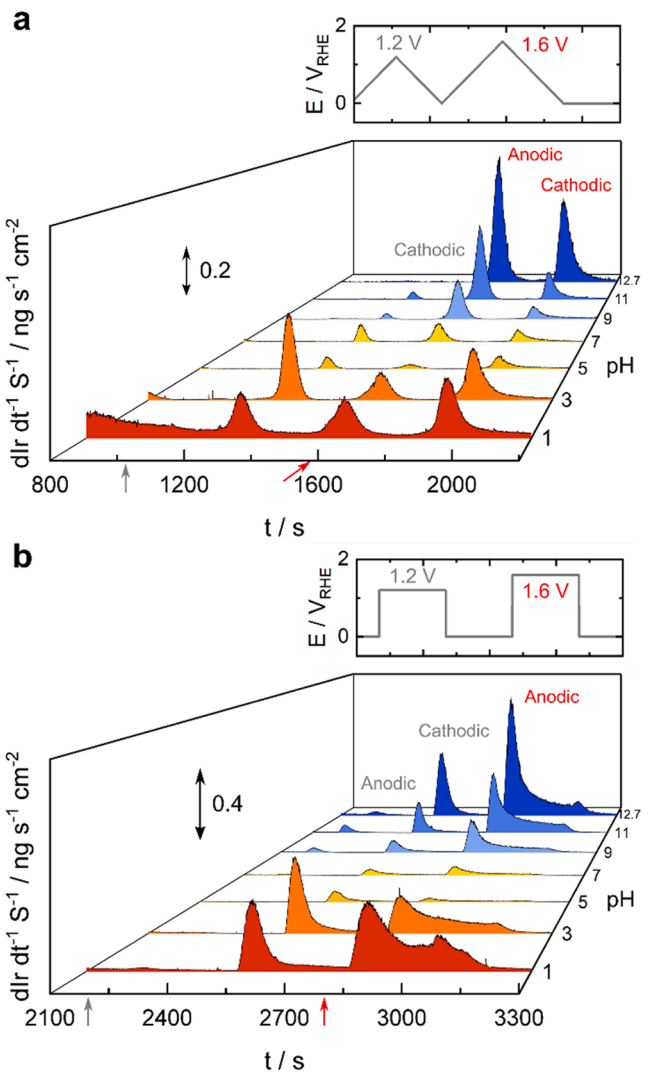

Fig. 4. Iridium dissolution profiles across different pH values measured by SFC-ICP-MS during: a) Slow CV scans up to 1.2 and 1.6 V_{RHE}, and b) Potentiostatic holds at 1.2 V_{RHE} and 1.6 V_{RHE}. In (a), gray and red arrows indicate the start of reverse scans, while in (b), they mark the start of potentiostatic holds.

0 V_{RHE} initially decreases up to pH 7, but then increases again until pH reaches 12.7.

Additionally, we evaluated the potential onsets of anodic and cathodic dissolution of iridium depending on pH, as shown in Figure S8. Anodic dissolution begins around 0.9 V_{RHE}, while cathodic dissolution starts around 0.1 V_{RHE}. Notably, these onsets remain consistent across different pH levels, except at pH 3, where both anodic and cathodic onsets are downshifted. Additionally, a second cathodic dissolution onset occurs around 0.9 V_{RHE} at pH 12.7. These values align with those reported in previous studies [4,15].

In the OER region at 1.6 V_{RHE}, we observe that anodic dissolution trends during the hold closely align with those obtained from the CVs. Specifically, Ir dissolution decreases up to pH 5 and then increases as conditions become more alkaline, reaching pH 12.7. Notably, at this potential, there is an overlap between anodic dissolution and the cathodic dissolution during the following 0 V_{RHE} hold. However, we have chosen to present the data as anodic dissolution only, as anodic dissolution remains the dominant mechanism of Ir dissolution at or above 1.6 V_{RHE} [4], while cathodic dissolution plays a comparatively minor role.

3.2. Stability under potentiodynamic and quasi steady-state conditions

To highlight the stability and dissolution trends more clearly, we integrated the area under the dissolution profiles from Fig. 4, presenting the results in Fig. 5.

3.2.1. Pre-OER region

As previously mentioned, anodic dissolution was generally absent during potential scans up to 1.2 V_{RHE} across most pH values. This is contradictory to a previous study by Cherevko et al. [13] where anodic dissolution during potential scans up to 1.2 V_{RHE} at pH 1, was observed. At pH 1, the anodic dissolution might have overlapped with the pronounced dissolution from the cleaning cycles preceding the CV (see Figure S6). However, this explanation might not be applicable for other pH values where the residual dissolution signal is either negligible or entirely absent.

We hypothesize that a native oxide layer might have formed on the Ir surface after polishing, which has been shown to increase with air exposure over time [95], or that the surface could partially oxidize following the cleaning cycles. To explore this possibility, we tested polycrystalline Ir using protocols without the initial cleaning CVs, setting LPLs to 0 and −0.1 V_{RHE}, as shown in Figure S9. The results indicate anodic dissolution during the anodic scan to 1.2 V_{RHE}, which becomes more pronounced and increases as the LPL is lowered. Additionally, the cathodic dissolution observed in following CV scans is lower without the cleaning CVs, suggesting a reduced presence of oxide on the surface or less rough oxide surface. Therefore, we conclude that the lack of anodic dissolution observed, compared to previous studies, could be attributed to the inclusion of cleaning CVs in our protocol. Nonetheless, we opted to include these cleaning CVs, in addition to polishing, to ensure a reproducible surface for each measurement. In contrast to the CVs, anodic dissolution is observed during potential hold at 1.2 V_{RHE}, with its extent increasing as pH rises, as seen in Fig. 5b. Interestingly, a clear threshold at pH 7 marks a shift from minimal dissolution in acidic conditions to more pronounced dissolution in alkaline environments.

In the reverse cathodic potential scan of the CV starting from 1.2 V_{RHE} (as shown in Fig. 5a), cathodic dissolution is observed. It increases as the pH changes from 1 to 3, but decreases as the pH becomes more alkaline.

The initial increase in dissolution observed between pH 1 and pH 3 (transitioning from non-buffered to buffered conditions) can be attributed to the influence of the phosphate buffer and the potential adsorption of phosphate species on the Ir surface. To investigate this further, we added 0.05 M H_3PO_4 to 0.1 M $HClO_4$ at pH 1, as shown in Figure S10a. The figure reveals that the addition of phosphates did not significantly affect cathodic dissolution during CV at an UPL of 1.2 V_{RHE}. However, both anodic and cathodic dissolution rates were substantially reduced at the higher UPL of 1.6 V_{RHE}.

Given the differing adsorption strengths and pK_a values of H_3PO_4 and $H_2PO_4^-$, fully explaining the observed increase in dissolution at pH 3 remains challenging. We further analyzed this effect by comparing buffered and unbuffered conditions at pH 3 without phosphates (Figure S10b). Similar to pH 1, we again observed higher dissolution in the phosphate electrolyte, likely due to the adsorption effect.

We extended this analysis to alkaline pH 12.7 with the addition of phosphates (Figure S10c). Although the dissolution appeared similar when normalized by surface area, it was lower when normalized by total anodic charge, as seen at pH 1. The exact mechanisms behind these adsorption effects are not yet fully understood and are beyond the scope of this study. This topic should be the focus of future research.

Furthermore, during the reverse potential scan in the CV, cathodic dissolution is lower compared to dissolution during potential holds at 0 V_{RHE} following a 1.2 V_{RHE} hold (Fig. 5c). In addition, differences arise after pH 7: while cathodic dissolution continues to decline in the CVs, it begins to increase during the potentiostatic holds.

3.2.2. OER region

Fig. 5d and e show the anodic dissolution of iridium in the OER region under potentiodynamic conditions (during CVs) and quasi-steady-state conditions (during holds). Integrating the dissolution profiles reveals a clear trend: anodic dissolution decreases up to pH 5, then increases through pH 12.7 under both conditions. However, the prolonged exposure within the OER region during holds allows for more dissolution cycles, resulting in notably higher iridium dissolution compared to CV [4,13].

Cathodic dissolution follows a similar trend to anodic dissolution, with a noticeable minimum at pH 7, as shown in Fig. 5d. Below pH 7, cathodic dissolution surpases anodic dissolution. However, this trend reverses above pH 7, with anodic dissolution becoming increasingly dominant, especially in alkaline media. This trend is consistent with previous results reported by Cherevko et al. [4] and Schalenbach et al. [15] Finally, Figure S11 presents a comparison of the total dissolution of Ir throughout the entire protocol between SFC-ICP-MS and RDE, showing a relatively good match between the two methods.

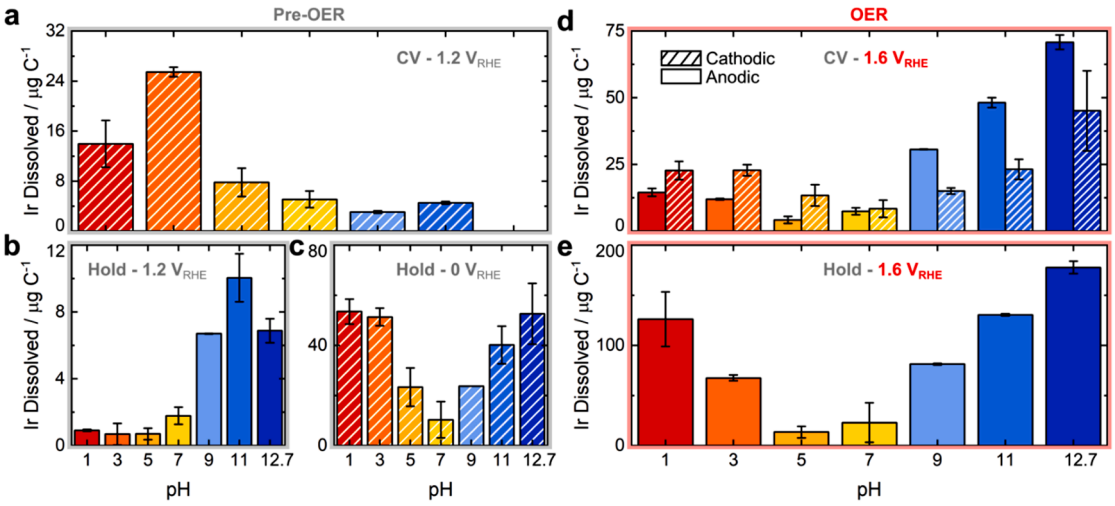

Fig. 5. Iridium stability as a function of pH. Quantification of: a) Cathodic dissolution during CV (1.2 – 0 V_{RHE}). b) Anodic dissolution during 1.2 V_{RHE} hold. c) Cathodic dissolution during 0 V_{RHE} hold. d) Anodic and cathodic dissolution during cyclic voltammetry between 0 and 1.6 V_{RHE} and d) Anodic dissolution during potentiostatic hold at 1.6 V_{RHE}. Dissolution profiles used for integrations are shown in Fig. 4.

3.3. pH-Dependent OER activity / stability

In the following section, we examine the relationship between OER activity and stability of Ir under varying pH conditions, using both SFC-ICP-MS and RDE setups. Our initial evaluation focuses on OER activity, where, in the first approach, Ir activity at 1.6 V_{RHE} was assessed using CV scans up to 1.6 V_{RHE} (Fig. 6a and c), analogous to linear sweep voltammetry (LSV). Since this method does not reflect steady-state conditions, the activity estimates may only partially represent actual catalytic behavior. To validate these trends more conclusively, we also analyzed the activity data following a 5-minute potentiostatic hold at 1.6 V_{RHE}, as shown in Figures S12a and S12b.

Overall, we observe a consistent trend in OER activity between the CVs and potentiostatic holds, as shown in Figs. 6c and S12b. The activity trend measured with CVs (Fig. 6c) follows the sequence: pH 1 > pH 3 > pH 12.7 > pH 7 > pH 9 > pH 5 > pH 11. Our findings also align well with the OER activity trends reported by Kuo et al. [56] (pH 1 > pH 2.8 ~ pH 12.9 > pH 6.5 > pH 9.6) and a recent study by Kumeda et al. [39], (pH 1.7 > pH 12.1 > pH 6.9 > pH 4.5 > pH 9.3) determined in phosphate buffer conditions using LSV. However, a difference is observed between pH 5 and pH 9 in the latter. In Kumeda's study, pH 5 showed higher activity compared to pH 9, while our results indicate the opposite. This deviation may arise from the differing experimental details used in the studies; we used polycrystalline Ir and 0.05 M phosphate buffers, whereas Kumeda's study involved single-crystal Ir(100) and 0.1 M phosphate buffer (leading to potential differences in buffer capacity).

Despite the complexity of the data, it is clear that OER activity is highest in unbuffered pH 1 conditions, with a noticeable drop in phosphate buffer, as also observed by Minguzzi et al. [26] However, the complexity increases when examining activity within the buffered media. Considering that data from the SFC is not iR drop-compensated, and as we stated in our previous publication [84], absolute currents in the SFC typically fall in the μA to nA range, making iR drop often negligible. This observation aligns with discussion of Bergmann et al., where it was stated that differences in activity trends in buffered media were not simply attributed to ionic (proton) conductivity of the electrolyte or iR compensation, as it did not change the trends [52]. To validate this, we also compare SFC data and trends with iR compensated RDE results, where the same trends are observable as shown in Figure S13. This is further supported by the addition of phosphates at pH 1 and 12.7, which results in a significant decrease in iridium activity at pH 1 and an increase at pH 12.7, suggesting a potential role of the buffer (Figure S14).

We now focus on analyzing Tafel slopes derived from the forward scan of LSVs (Fig. 6a), presented in Fig. 6b. To provide a clearer representation, the logarithmic scale of LSVs is also plotted in Figure S15. Variations in Tafel slopes, among other factors, are classically ascribed to changes in OER mechanisms. Higher Tafel slopes observed at high overpotential region in buffered conditions, as also noted by Kumeda et al. [39], could stem from factors such as bubble formation, conductivity influences, or subsequent chemical steps following electrochemical ones. Another plausible explanation involves mass transport limitations due to the diffusion of protonated or unprotonated buffer bases within the electrolyte, affecting its buffering capacity [57], discussed later.

Tafel slope values vary significantly with pH, generally increasing, but with noticeable decreases at the pH transitions around 5 and 9. At pH 1, the value of approximately 59.5 mV dec^{-1} corresponds to the rate-determining step involving dissociation of the OH surface complex [4, 39,96]. At pH 3, the increase in Tafel slope to ~87.5 mV dec^{-1} is likely due to strong phosphate adsorption affecting OH_{ads} and O_{ads} adsorption, thus influencing this first proton-coupled electron transfer (PCET) step. At near-neutral and neutral pH levels, the Tafel slope is influenced by mass transport of OH^- or O_2, primarily influenced by buffer species (A^-). Notably, at pH 9, the Tafel slope increases to 122 mV dec^{-1}, corresponding to the first PCET step ($OH_{ad} \rightarrow OH_{ad} + e^-$), likely due to a reduced rate of OH^- supply and its lower availability, which aligns with lower Tafel slopes at higher pH.

The observed decreases in Tafel slopes at transitions around pH 5 and pH 9 align with findings by Nishimoto et al. [55], who also noted similar transitions near pH 5 and 10, particularly at near-neutral pH values. Furthermore, Dau et al.'s calculations indicated a minimum Tafel slope at pH 7, spanning from pH 5 to 9 [57]. This transition coincides with the changes in composition of phosphate species, shifting from predominantly H_3PO_4 / $H_2PO_4^-$ in acidic conditions to $H_2PO_4^-$ / HPO_4^{2-} at pH 5 and HPO_4^{2-} / PO_4^{3-} at pH 10.

When overpotentials are plotted as a function of pH (Fig. 6d), they generally follow the phosphate titration curve in near-neutral and

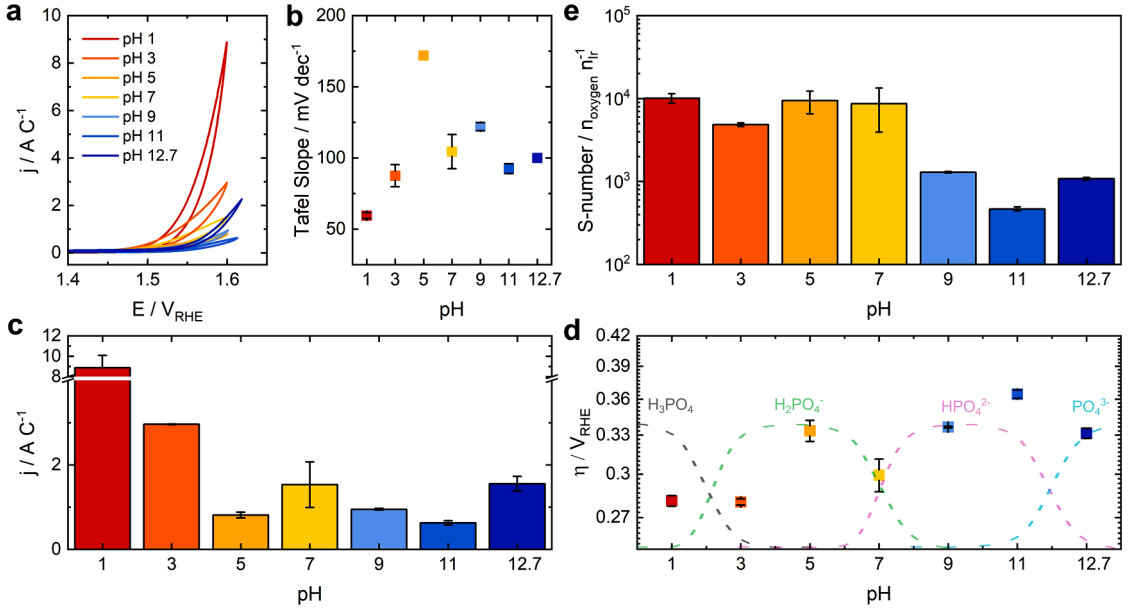

Fig. 6. Impact of pH on iridium's OER activity and stability. a) Cuts from CV scans from 0 to 1.6 V_{RHE}. b) Tafel slopes derived from CV data in a). c) OER activity at 1.6 V_{RHE} (derived from CV scan to 1.6 V_{RHE} UPL). d) OER overpotentials at 0.5 A C^{-1} depending on pH, derived from data in a). e) Stability numbers calculated from dissolution and charge at 1.6 V_{RHE} potentiostatic holds.

neutral conditions, reaching a minimum at the pK_a of phosphate where buffering is most effective. However, deviations are observed at extreme pH values (pH 3 and 11) [52,55].

To gain more insights about iridium stability during potentiostatic holds, we calculated the S-number, which reflects the ratio of oxygen evolution to Ir dissolution [22]. Notably, two distinct stability regions based on pH are observed: acidic / neutral (pH $\leq$ 7) and alkaline (pH > 7) (Fig. 6e and S16). The boundary between these regions appears to differ slightly between the techniques employed (RDE vs. SFC-ICP-MS). As seen in Fig. 5e, iridium demonstrates significantly higher stability (higher S-number) in acidic and neutral conditions than in alkaline environments, consistent with the RDE data presented in Figure S16. Additionally, a decrease in stability is also observed when transitioning from unbuffered media at pH 1 to buffered conditions at pH 3. This observation contrasts with Knoppel et al.'s findings, where increased Ir stability with rising pH was reported [21]. We will discuss this discrepancy in more detail later. Similar transition was also observed when moving from pH 11 to 12.7, again when switching between buffered and unbuffered conditions. For more information regarding the effect of the electrolyte on the OER activity / stability of Ir black, see Section S4 in SI.

4. Discussion

4.1. Pre-OER region

Dissolution of iridium under pre-OER conditions primarily involves the dissolution of short-lived, unstable intermediate oxide / hydroxide phases. These phases form during transitions between two stable phases under non-equilibrium potential changes [13]. This includes two distinct transient dissolution processes: anodic and cathodic. Anodic dissolution takes place during oxide formation through electro-adsorption of OH and interfacial place-exchange [97,98], while cathodic dissolution occurs during oxide reduction, similar to other noble metals [99–102]. We show that both processes are depending on pH, and will discuss them in relation to thermodynamic predictions indicated by Pourbaix diagram (Fig. 3) [91]. In addition, dissolution trends differ between potentiodynamic or potentiostatic conditions, indicating role of kinetics, not accounted in thermodynamics.

While anodic dissolution was negligible during potential scans (Fig. 4a), it became noticeable under potentiostatic conditions. In particular, dissolution was minimal in acidic media but significant in alkaline media, with a clear pH threshold around 7 (Fig. 5b). The absence of anodic dissolution during potential scans across most pH values likely results from the formation of native oxide during electrode preparation [95], or surface oxidation during cleaning cycles (Fig. 1 and S6). This is evidenced by the increase in anodic dissolution with decreasing LPL or removing cleaning cycles (Figure S9). Additionally, as discussed in Section S2 in SI, phosphate adsorption cannot be excluded. Starting around 0.3 V_{RHE} [39], it potentially competes with OH adsorption (initiating at 0.4 – 0.5 V_{RHE}) [13], inhibiting the formation of Ir^{3+} and IrO_2 or shifting their formation to higher potentials [103]. This is similar to the previously observed inhibition of OH adsorption and anodic dissolution on platinum due to CO adsorption [102].

While anodic dissolution becomes evident under potentiostatic conditions (Fig. 5b), it is presumably influenced by several factors. At the relatively low potentials, processes such as place-exchange and oxygen coverage increase are kinetically hindered. Hence, the rate of these processes is influenced by the timescale of the experiment [13], with the probability of place-exchange events increasing over time [104].

Given the short duration and low potential applied during the potential scans, these conditions are generally insufficient for replacing adsorbed phosphates with OH or O groups or facilitating place-exchange, a process further hindered by the presence of a native oxide layer. This aligns with study by Breiter [105], who observed a good correlation between experimentally obtained iridium voltammograms and those computed for OH and O adsorption under Langmuir conditions. The Langmuir adsorption isotherm describes adsorption at specific homogeneous sites on a surface, where the availability of unoccupied sites limits the extent of adsorption. Once all sites are occupied, no additional adsorption can occur until previously adsorbed species are displaced or removed. This saturation effect restricts further OH adsorption, slowing down the place-exchange mechanism and rendering it improbable under potentiodynamic conditions.

The extended duration of potentiostatic holds overcomes kinetic barriers, resulting in observable anodic dissolution. However, dissolution is less pronounced in acidic conditions and increases significantly at higher pH values (Fig. 5b). This can be attributed to the weakened adsorption of phosphate anions in alkaline environments, as proposed by Kumeda et al. [39] With reduced phosphate adsorption, the place-exchange mechanism becomes more pronounced, as discussed in the previous paragraph. Additionally, thermodynamic considerations from the Pourbaix diagram [91] indicate that the formation of IrO_4^{2-} is favored at higher pH values, while IrO_2 remains stable at lower pH at 1.2 V_{RHE}. Therefore, the interplay between thermodynamics, influenced by pH and kinetics (related to timescale and potential), ultimately determines the anodic dissolution behavior. However, the role of adsorbed phosphates in this dynamic also cannot be overlooked.

Cathodic dissolution trends, similar to anodic, show differences between potentiodynamic and potentiostatic conditions (Fig. 5a and c). Both trends typically show a decrease in cathodic dissolution as pH increases, consistent with the stability of Ir^{3+} species in acidic conditions, according to the Pourbaix diagram (Fig. 3) [91]. This suggests potential redeposition of Ir^{3+} at neutral to slightly alkaline pH values, leading to lower observed dissolution rates, similar to observations in our previous studies on pH-dependent Pt dissolution [82] and Ir on Au backing electrode [84], where redeposition was influenced by experimental conditions. However, the increase in dissolution at higher pH levels remains unexplained and indicates the presence of unidentified ionic specie, not reflected in Pourbaix diagram. This observation is similar to results from our previous pH study on platinum [82]. More in-depth investigations are necessary to accurately identify these species and improve our understanding of iridium dissolution, in line with recent advancements on Pt oxide [106].

Finally, a notable outlier was observed in cathodic dissolution at pH 3 during potential scans (Fig. 5a). Although the general trend shows decreasing cathodic dissolution with increasing pH, consistent with the stability of Ir^{3+} species as outlined in the Pourbaix diagram, the unusual behavior at pH 3 suggests other influencing factors. This is also evidenced by shifts in the onset potentials of both anodic and cathodic dissolution at this pH (Figure S8). Assuming the place-exchange mechanism during oxide formation (pH independent on RHE scale) contributes to dissolution, the pH-independent shifts in onset potentials are expected [106]. Thus, the interactions between phosphate adsorption and oxide formation also requires further study to clarify the underlying mechanisms involved.

4.2. OER region

In the OER region (up to 1.6 V_{RHE}), dissolution is predominantly driven by OER mechanisms, depending on reaction kinetics [4]. It has been proposed that OER and iridium dissolution share common intermediates [93], resulting in continuous shifts in the oxidation states [94], and leading to steady-state dissolution. Previous studies have largely focused on dissolution in extreme acidic or alkaline environments [4,18,21], leaving the broader pH spectrum relatively unexplored.

Our detailed analysis in Section S5 of the SI suggests that OH^- is the primary reactant in near-neutral media, particularly under buffering conditions, where the pK_a aligns closely with the pH. This allows us to outline several OER mechanisms across different pH regions, with corresponding reactions as follows:

1) Acidic OER [36]:

$2H_2O \rightarrow 4H^+ + 4e^- + O_2$ ($E^\circ = 1.23$ V vs. SHE)

2) Buffered near-neutral OER [48,53,55]:

2.1 OH^- generation by buffer species

$H_2O + A^- \rightarrow OH^- + HA$

$HA \rightarrow H^+ + A^-$

$4OH^- \rightarrow O_2 + 2H_2O + 4e^-$

2.2 Proton removal facilitated by buffer species

$2H_2O + 4A^- \rightarrow O_2 + 4HA + 4e^-$

3) Alkaline OER [36]:

$4OH^- \rightarrow O_2 + 2H_2O + 4e^-$ ($E^\circ = 0.40$ V vs. SHE)

With all factors considered, the OER activity of iridium is dependent not only on the specific OER mechanism prevalent in different pH regions but also by the type and concentration of reactants and the electrolyte type, as discussed above. We will now interpret the observed activity-stability trends in terms of pH-dependent OER mechanisms.

As pH increases from acidic to mildly neutral, we observe a decrease in both the activity and dissolution of iridium (Figs. 6c and 5e). The decline in activity from pH 1 to pH 3 can be attributed to a higher formation barrier of the OOH_{ad} intermediate [56]. In near-neutral and neutral media, OER activity is dependent on the availability of OH^-, which is maximized as the pH approaches the pK_a of the buffer (pK_a = 7.2 in this case), resulting in lower activity at pH 5 and an increased at pH 7. Correspondingly, dissolution rates decrease until pH 5 and increase again at pH 7.

A similar dissolution trend was observed for cathodic dissolution under pre-OER conditions, attributed to the potential redeposition of formed Ir^{3+} species, whose stability window decreases with pH, as predicted by the Pourbaix diagram [91]. However, this explanation does not hold in the OER region, as evidenced by the constant S-numbers, regardless of pH (Fig. 6e). Therefore we must consider the OER dissolution mechanism summarized by Kasian et al. [93] suggesting two potential-dependent pathways for iridium dissolution in acidic conditions. One at high anodic potentials (> 1.6 V_{RHE}) and another at lower potentials. We propose that these pathways are also pH-dependent. Specifically, the lower potential pathway involving the formation of Ir^{3+} species predominating in acidic media. Therefore, constant S-numbers around 10^4, suggests that for every 10^4 intermediates formed during OER cycle, one active site dissolves as Ir^{3+}, independently of pH from acidic to neutral conditions.

This observation contradicts the proposed pH-dependent formation of Ir^{3+} and IrO_2 during OER cycles, according to the reactions [93]:

$HIrO_2 + 3H^+ \rightarrow Ir^{3+} + 2H_2O$

$HIrO_2 \rightarrow IrO_2 + H^+ + e^-$

These reactions would predict lower dissolution rates in less acidic conditions. However, the constant S-numbers, regardless of pH (Fig. 6e), suggest that OER activity and dissolution rates are equally impacted by the pH.

Previously, Naito et al. [54] suggested that the improved stability of iridium in neutral buffered conditions might be attributed to a self-healing mechanism similar to that observed in Co-phosphate systems during OER [107–109]. Although the solubility product (K_{sp}) of an Ir(III)-phosphate complex remains undetermined, its potential similarity to Co-phosphate (owing to their shared periodic group and d-electron characteristics), could suggest comparably low K_{sp} values. If this were the case, dissolved Ir(III)-phosphate would redeposit on the electrode surface, as previously reported for iridium-based perovskites [110]. However, such a mechanism would presumably lead to decreased dissolution rates at the same OER activity, resulting in increased stability numbers compared to acidic conditions, which we did not observe in this study.

Beyond pH 9, particularly up to pH 11, there's a further decrease in activity due to a shift in the OER mechanism towards OH^- as the primary reactant, influenced by its concentration in the electrolyte (Fig. 6c). This trend aligns with the OER overpotential versus pH curve (Fig. 6b), which mirrors the titration curve of phosphate buffer [52,55]. This is accompanied by further increase of iridium dissolution from pH 7 to pH 12.7 (Fig. 5e).

We again correlate this to proposed dissolution mechanism [93]. The dissolution pathway from Ir^V to Ir^{VI}, which is proposed to occur at higher anodic potentials in acidic conditions, could also dominate the dissolution at lower potentials in alkaline conditions [93]. This can be explained considering previous reports suggesting that IrO_3 is relatively stable in alkaline electrolytes but decomposes in dilute sulfuric acid with simultaneous O_2 evolution [111]. Since the hydrolysis of IrO_3 potentially has slower kinetics compared to its decomposition [93], its better stability in alkaline media could lead to a preferential pathway involving hydrolysis and the formation of IrO_4^{2-} ions rather than decomposition. This aligns with the Pourbaix diagram predictions for these conditions [91].

Therefore, we hypothesize that the observed decrease in S-numbers from pH 7 to pH 11 (Fig. 6e) results from concurrent dissolution mechanisms involving both the formation of Ir^{3+} and IrO_4^{2-}. At pH 12.7, the dissolution appears to be governed predominantly by a single

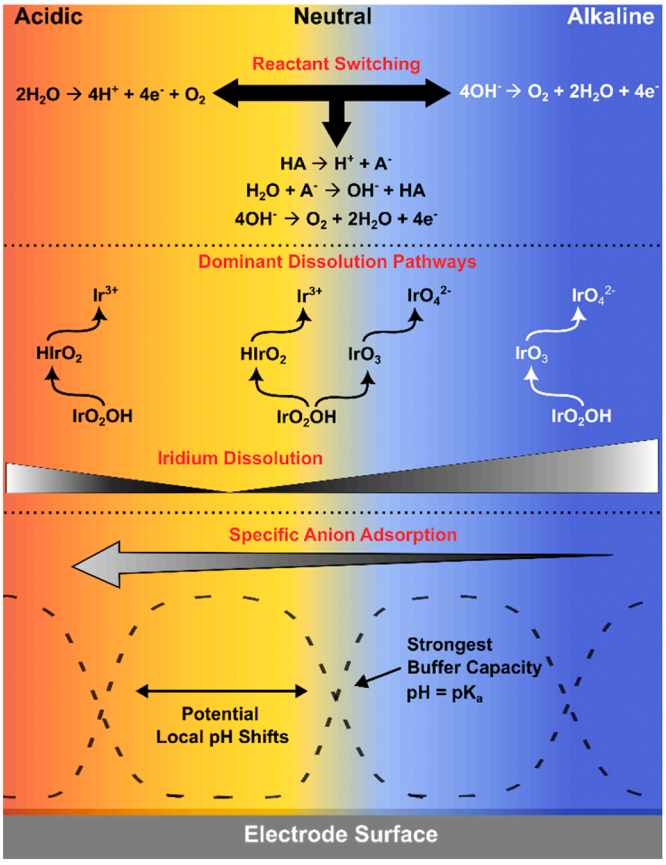

Fig. 7. Overview of pH-dependent mechanisms affecting iridium's OER activity and stability in buffered conditions.

mechanism, as observed by increase in S-number.

A summary of the OER mechanisms depending on pH and the role of buffer species, as discussed above, is provided in Fig. 7 for easier interpretation.

Finally, it is important to note outlier in stability numbers at pH 3 (Fig. 6e). The decline at pH 3 contrasts with an earlier study that reported increased stability at higher pH values in acidic conditions [21]. The discrepancy could stem from differences in the electrolytes used (see Figure S14b). Whereas the previous study was conducted in unbuffered media, which could allow local pH fluctuations, our experiments utilized buffered solutions. Additionally, the presence of phosphate buffers in our setup may influence iridium stability through specific adsorption interactions on the Ir surface [38,39]. Similar effects were observed in our study under pre-OER conditions at pH 3. Further research is important to fully understand this phenomenon, which holds significant implications for practical application.

5. Conclusion

This study systematically investigated the stability and dissolution mechanisms of iridium across a broad pH spectrum, under both pre-OER and OER conditions.

In the pre-OER region:

- Phosphate ions adsorb on the iridium surface, influencing the pH-dependent shifts in the Ir^{III} / Ir^{IV} redox transition potential.
- Anodic dissolution is influenced by native oxide formation, kinetic limitations, and phosphate adsorption.
- Kinetic factors play a critical role in dissolution behavior, showing the limitations of only thermodynamic models.
- The presence of previously unidentified species resulting from cathodic dissolution in alkaline conditions is proposed.

In the OER region:

- Both OER activity and stability are pH dependent, with proposed mechanisms varying by pH:
  - In acidic to neutral conditions, dissolution is mainly driven by the formation of Ir^{3+}.
  - As conditions shift to slightly alkaline, the formation of IrO_4^{2-} contributes to decreased stability.
  - In strongly alkaline media, dissolution becomes dominated by IrO_4^{2-}, leading to increased dissolution.
- Phosphate ions appear to influence iridium stability during OER, requiring further study.
- Buffers help maintain a stable local pH depending on buffer capacity, with mechanism changing depending on pH.
- Iridium's stability extends to neutral pH, suggesting its potential for applications in various electrochemical systems, including seawater electrolysis.

These insights, as well as the role of buffers in stabilizing local pH, hold potential for optimizing the performance and durability of iridium-based catalysts, leading to more durable and efficient electrochemical devices. Similar pH effects were observed with other noble metals such as platinum [82] and gold [81], recently published.

CRediT authorship contribution statement

Matej Zlatar: Writing – original draft, Visualization, Validation, Methodology, Investigation, Formal analysis, Data curation, Conceptualization. **Daniel Escalera-López:** Writing – review & editing. **Cornelius Simon:** Investigation. **Valentín Briega-Martos:** Writing – review & editing, Validation, Methodology, Conceptualization. **Kevin Stojanovski:** Writing – review & editing, Validation, Methodology, Conceptualization. **Serhiy Cherevko:** Writing – review & editing, Supervision, Resources, Project administration, Methodology, Funding acquisition, Conceptualization.

Declaration of competing interest

The authors declare that they have no known competing financial interests or personal relationships that could have appeared to influence the work reported in this paper.

Supplementary materials

Supplementary material associated with this article can be found, in the online version, at doi:10.1016/j.electacta.2024.145450.

Data availability

Data will be made available on request.

References

[1] International Energy Agency, World Energy Outlook 2022. https://www.iea.org/reports/world-energy-outlook-2022 (accessed 2023.
[2] J. Rossmeisl, A. Logadottir, J.K. Nørskov, Electrolysis of water on (oxidized) metal surfaces, Chem. Phys. 319 (1) (2005) 178–184, https://doi.org/10.1016/j.chemphys.2005.05.038.
[3] I.C. Man, H.-Y. Su, F. Calle-Vallejo, H.A. Hansen, J.I. Martínez, N.G. Inoglu, J. Kitchin, T.F. Jaramillo, J.K. Nørskov, J. Rossmeisl, Universality in oxygen evolution electrocatalysis on oxide surfaces, ChemCatChem. 3 (7) (2011) 1159–1165, https://doi.org/10.1002/cctc.201000397.
[4] S. Cherevko, A.R. Zeradjanin, A.A. Topalov, N. Kulyk, I. Katsounaros, K.J. J. Mayrhofer, Dissolution of noble metals during oxygen evolution in acidic media, ChemCatChem. 6 (8) (2014) 2219–2223, https://doi.org/10.1002/cctc.201402194.
[5] M. Clapp, C.M. Zalitis, M. Ryan, Perspectives on current and future iridium demand and iridium oxide catalysts for PEM water electrolysis, Catal. Today 420 (2023) 114140, https://doi.org/10.1016/j.cattod.2023.114140.
[6] C. Minke, M. Suermann, B. Bensmann, R. Hanke-Rauschenbach, Is iridium demand a potential bottleneck in the realization of large-scale pem water electrolysis? Int. J. Hydrogen Energy 46 (46) (2021) 23581–23590, https://doi.org/10.1016/j.ijhydene.2021.04.174.
[7] R.R. Beswick, A.M. Oliveira, Y. Yan, Does the green hydrogen economy have a water problem? ACS Energy Lett. 6 (9) (2021) 3167–3169, https://doi.org/10.1021/acsenergylett.1c01375.
[8] J.S. Murawski, Soren, R. Rao, K. Rigg, C. Zalitis, J. Stevens, J. Sharman, G. Hinds, I.E.L. Stephens, Benchmarking Stability of IrOx in Acidic Media Under O2 Evolution Conditions: A Review, Johnson Matthey Technology Review, 2023, https://doi.org/10.1595/205651323X16848455435118.
[9] J.S. Ko, J.K. Johnson, P.I. Johnson, Z. Xia, Decoupling oxygen and chlorine evolution reactions in seawater using iridium-based electrocatalysts, ChemCatChem. 12 (18) (2020) 4526–4532, https://doi.org/10.1002/cctc.202000653.
[10] J.G. Vos, Z. Liu, F.D. Speck, N. Perini, W. Fu, S. Cherevko, M.T.M. Koper, Selectivity trends between oxygen evolution and chlorine evolution on iridium-based double perovskites in acidic media, ACS Catal. 9 (9) (2019) 8561–8574, https://doi.org/10.1021/acscatal.9b01159.
[11] L. Moriau, K. Stojanovski, P. Jovanovič, D. Escalera-López, S. Cherevko, N. Hodnik, Towards electrochemical iridium recycling in acidic media: effect of the presence of organic molecules and chloride ions, RSC Adv. 13 (12) (2023) 7980–7987, https://doi.org/10.1039/D2RA07142H.
[12] D. Escalera-López, S. Czioska, J. Geppert, A. Boubnov, P. Röse, E. Saraçi, U. Krewer, J.-D. Grunwaldt, S. Cherevko, Phase- and Surface composition-dependent electrochemical stability of Ir-Ru nanoparticles during oxygen evolution reaction, ACS Catal. 11 (15) (2021) 9300–9316, https://doi.org/10.1021/acscatal.1c01682.
[13] S. Cherevko, S. Geiger, O. Kasian, A. Mingers, K.J.J. Mayrhofer, Oxygen evolution activity and stability of iridium in acidic media. Part 1. – metallic iridium, J. Electroanal. Chem. 773 (2016) 69–78, https://doi.org/10.1016/j.jelechem.2016.04.033.
[14] S. Cherevko, S. Geiger, O. Kasian, A. Mingers, K.J.J. Mayrhofer, Oxygen evolution activity and stability of iridium in acidic media. Part 2. – electrochemically grown hydrous iridium oxide, J. Electroanal. Chem. 774 (2016) 102–110, https://doi.org/10.1016/j.jelechem.2016.05.015.
[15] M. Schalenbach, O. Kasian, M. Ledendecker, F.D. Speck, A.M. Mingers, K.J. J. Mayrhofer, S. Cherevko, The electrochemical dissolution of noble metals in alkaline media, Electrocatalysis 9 (2) (2018) 153–161, https://doi.org/10.1007/s12678-017-0438-y.
[16] L. Wan, Z. Xu, Q. Xu, M. Pang, D. Lin, J. Liu, B. Wang, Key components and design strategy of the membrane electrode assembly for alkaline water electrolysis, Energy Environ. Sci. 16 (4) (2023) 1384–1430, https://doi.org/10.1039/D3EE00142C.

[17] Z. Li, G. Lin, L. Wang, H. Lee, J. Du, T. Tang, G. Ding, R. Ren, W. Li, X. Cao, S. Ding, W. Ye, W. Yang, L. Sun, Seed-assisted formation of NiFe anode catalysts for anion exchange membrane water electrolysis at industrial-scale current density, Nat. Catal. (2024), https://doi.org/10.1038/s41929-024-01209-1.
[18] S. Cherevko, S. Geiger, O. Kasian, N. Kulyk, J.-P. Grote, A. Savan, B.R. Shrestha, S. Merzlikin, B. Breitbach, A. Ludwig, K.J.J Mayrhofer, Oxygen and hydrogen evolution reactions on ru, ruo2, ir, and iro2 thin film electrodes in acidic and alkaline electrolytes: a comparative study on activity and stability, Catal. Today 262 (2016) 170–180, https://doi.org/10.1016/j.cattod.2015.08.014.
[19] Y. Lee, J. Suntivich, K.J. May, E.E. Perry, Y. Shao-Horn, Synthesis and activities of rutile IrO2 and RuO2 nanoparticles for oxygen evolution in acid and alkaline solutions, J. Phys. Chem. Lett. 3 (3) (2012) 399–404, https://doi.org/10.1021/jz2016507.
[20] C. Liang, Y. Katayama, Y. Tao, A. Morinaga, B. Moss, V. Celorrio, M. Ryan, I.E. L. Stephens, J.R. Durrant, R.R. Rao, Role of electrolyte pH on water oxidation for iridium oxides, J. Am. Chem. Soc. 146 (13) (2024) 8928–8938, https://doi.org/10.1021/jacs.3c12011.
[21] J. Knöppel, M. Möckl, D. Escalera-López, K. Stojanovski, M. Bierling, T. Böhm, S. Thiele, M. Rzepka, S. Cherevko, On the limitations in assessing stability of oxygen evolution catalysts using aqueous model electrochemical cells, Nat. Commun. 12 (1) (2021) 2231, https://doi.org/10.1038/s41467-021-22296-9.
[22] S. Geiger, O. Kasian, M. Ledendecker, E. Pizzutilo, A.M. Mingers, W.T. Fu, O. Diaz-Morales, Z. Li, T. Oellers, L. Fruchter, A. Ludwig, K.J.J. Mayrhofer, M.T. M. Koper, S. Cherevko, The stability number as a metric for electrocatalyst stability benchmarking, Nat. Catal. 1 (7) (2018) 508–515, https://doi.org/10.1038/s41929-018-0085-6.
[23] R.I. Masel, Z. Liu, H. Yang, J.J. Kaczur, D. Carrillo, S. Ren, D. Salvatore, C. P. Berlinguette, An industrial perspective on catalysts for low-temperature CO2 electrolysis, Nat. Nanotechnol. 16 (2) (2021) 118–128, https://doi.org/10.1038/s41565-020-00823-x.
[24] Á. Vass, B. Endrődi, G.F. Samu, Á. Balog, A. Kormányos, S. Cherevko, C. Janáky, Local chemical environment governs anode processes in CO2 electrolyzers, ACS Energy Lett. 6 (11) (2021) 3801–3808, https://doi.org/10.1021/acsenergylett.1c01937.
[25] L. Giordano, B. Han, M. Risch, W.T. Hong, R.R. Rao, K.A. Stoerzinger, Y. Shao-Horn, pH dependence of OER activity of oxides: current and future perspectives, Catal. Today 262 (2016) 2–10, https://doi.org/10.1016/j.cattod.2015.10.006.
[26] A. Minguzzi, F.-R.F. Fan, A. Vertova, S. Rondinini, A.J. Bard, Dynamic potential–pH diagrams application to electrocatalysts for water oxidation, Chem. Sci. 3 (1) (2012) 217–229, https://doi.org/10.1039/C1SC00516B.
[27] M. Auinger, I. Katsounaros, J.C. Meier, S.O. Klemm, P.U. Biedermann, A. A. Topalov, M. Rohwerder, K.J.J. Mayrhofer, Near-surface ion distribution and buffer effects during electrochemical reactions, Phys. Chem. Chem. Phys. 13 (36) (2011) 16384–16394, https://doi.org/10.1039/C1CP21717H.
[28] M.T.M. Koper, Theory of multiple proton–electron transfer reactions and its implications for electrocatalysis, Chem. Sci. 4 (7) (2013) 2710–2723, https://doi.org/10.1039/C3SC50205H.
[29] V.J. Ovalle, M.M. Waegele, Influence of pH and proton donor/acceptor identity on electrocatalysis in aqueous media, J. Phys. Chem. C 125 (34) (2021) 18567–18578, https://doi.org/10.1021/acs.jpcc.1c05921.
[30] M.-K. Zhang, W. Chen, M.-L. Xu, Z. Wei, D. Zhou, J. Cai, Y.-X. Chen, How buffers resist electrochemical reaction-induced pH shift under a rotating disk electrode configuration, Anal. Chem. 93 (4) (2021) 1976–1983, https://doi.org/10.1021/acs.analchem.0c03033.
[31] I. Katsounaros, J.C. Meier, S.O. Klemm, A.A. Topalov, P.U. Biedermann, M. Auinger, K.J.J. Mayrhofer, The effective surface pH during reactions at the solid–liquid interface, Electrochem. Commun. 13 (6) (2011) 634–637, https://doi.org/10.1016/j.elecom.2011.03.032.
[32] J.A. Arminio-Ravelo, A.W. Jensen, K.D. Jensen, J. Quinson, M. Escudero-Escribano, Electrolyte effects on the electrocatalytic performance of iridium-based nanoparticles for oxygen evolution in rotating disc electrodes, Chemphyschem. 20 (22) (2019) 2956–2963, https://doi.org/10.1002/cphc.201900902.
[33] G.-F. Li, M. Divinagracia, M.F. Labata, J.D. Ocon, P.-Y. Abel Chuang, Electrolyte-Dependent oxygen evolution reactions in alkaline media: electrical double layer and interfacial interactions, ACS Appl. Mater. Interfaces 11 (37) (2019) 33748–33758, https://doi.org/10.1021/acsami.9b06889.
[34] J. Suntivich, E.E. Perry, H.A. Gasteiger, Y. Shao-Horn, The influence of the cation on the oxygen reduction and evolution activities of oxide surfaces in alkaline electrolyte, Electrocatalysis 4 (1) (2013) 49–55, https://doi.org/10.1007/s12678-012-0118-x.
[35] R.R. Rao, B. Huang, Y. Katayama, J. Hwang, T. Kawaguchi, J.R. Lunger, J. Peng, Y. Zhang, A. Morinaga, H. Zhou, H. You, Y. Shao-Horn, pH- and Cation-Dependent water oxidation on rutile RuO2(110), J. Phys. Chem. C 125 (15) (2021) 8195–8207, https://doi.org/10.1021/acs.jpcc.1c00413.
[36] J.C. Fornaciari, L.-C. Weng, S.M. Alia, C. Zhan, T.A. Pham, A.T. Bell, T. Ogitsu, N. Danilovic, A.Z. Weber, Mechanistic understanding of pH effects on the oxygen evolution reaction, Electrochim. Acta 405 (2022) 139810, https://doi.org/10.1016/j.electacta.2021.139810.
[37] T. Nishimoto, T. Shinagawa, T. Naito, K. Takanabe, Microkinetic assessment of electrocatalytic oxygen evolution reaction over iridium oxide in unbuffered conditions, J. Catal. 391 (2020) 435–445, https://doi.org/10.1016/j.jcat.2020.09.007.
[38] L.-E. Owe, M. Tsypkin, S. Sunde, The effect of phosphate on iridium oxide electrochemistry, Electrochim. Acta 58 (2011) 231–237, https://doi.org/10.1016/j.electacta.2011.09.043.
[39] T. Kumeda, K. Sakaushi, Joint kinetic/in situ spectrometric investigation of the multielectron/multiproton-transfer-based adsorption electrode process of phosphate anions on the ir(111) surface across a comprehensive pH range, J. Phys. Chem. C 127 (21) (2023) 10341–10354, https://doi.org/10.1021/acs.jpcc.3c01287.
[40] S.A.K. Navodye, G.T.K.K. Gunasooriya, Acid electrolyte anions adsorption effects on IrO2 electrocatalysts for oxygen evolution reaction, J. Phys. Chem. C 128 (14) (2024) 6041–6052, https://doi.org/10.1021/acs.jpcc.3c08103.
[41] I.S.P. Savizi, M.J. Janik, Acetate and phosphate anion adsorption linear sweep voltammograms simulated using density functional theory, Electrochim. Acta 56 (11) (2011) 3996–4006, https://doi.org/10.1016/j.electacta.2011.02.013.
[42] R. Gisbert, G. García, M.T.M. Koper, Adsorption of phosphate species on poly-oriented pt and pt(111) electrodes over a wide range of pH, Electrochim. Acta 55 (27) (2010) 7961–7968, https://doi.org/10.1016/j.electacta.2010.04.009.
[43] Perales-Rondón, J.V.; Brimaud, S.; Solla-Gullón, J.; Herrero, E.; Jürgen Behm, R.; Feliu, J.M. Further insights into the formic acid oxidation mechanism on platinum: pH and anion adsorption effects. *Electrochimica Acta* 2015, 180, 479–485. DOI: https://doi.org/10.1016/j.electacta.2015.08.155.
[44] G.A.B. Mello, V. Briega-Martos, V. Climent, J.M. Feliu, Bromide adsorption on Pt (111) over a wide range of pH: cyclic voltammetry and Co displacement experiments, J. Phys. Chem. C 122 (32) (2018) 18562–18569, https://doi.org/10.1021/acs.jpcc.8b05685.
[45] W. Sheng, Z. Zhuang, M. Gao, J. Zheng, J.G. Chen, Y. Yan, Correlating hydrogen oxidation and evolution activity on platinum at different pH with measured hydrogen binding energy, Nat. Commun. 6 (1) (2015) 5848, https://doi.org/10.1038/ncomms6848.
[46] M.N. Jackson, O. Jung, H.C. Lamotte, Y. Surendranath, Donor-Dependent promotion of interfacial proton-coupled electron transfer in aqueous electrocatalysis, ACS Catal. 9 (4) (2019) 3737–3743, https://doi.org/10.1021/acscatal.9b00056.
[47] H. Hashiba, L.-C. Weng, Y. Chen, H.K. Sato, S. Yotsuhashi, C. Xiang, A.Z. Weber, Effects of electrolyte buffer capacity on surface reactant species and the reaction rate of CO2 in electrochemical CO2 reduction, J. Phys. Chem. C 122 (7) (2018) 3719–3726, https://doi.org/10.1021/acs.jpcc.7b11316.
[48] G. Marcandalli, M.C.O. Monteiro, M.T.M. Koper, Electrolyte buffering species as oxygen donor shuttles in Co electrooxidation, Phys. Chem. Chem. Phys. 24 (4) (2022) 2022–2031, https://doi.org/10.1039/D1CP05030C.
[49] K. Obata, L. Stegenburga, K. Takanabe, Maximizing hydrogen evolution performance on Pt in buffered solutions: mass transfer constrains of H2 and buffer ions, J. Phys. Chem. C 123 (35) (2019) 21554–21563, https://doi.org/10.1021/acs.jpcc.9b05245.
[50] Z. Chen, J.J. Concepcion, X. Hu, W. Yang, P.G. Hoertz, T.J. Meyer, Concerted O atom—proton transfer in the O—O bond forming step in water oxidation, in: Proceedings of the National Academy of Sciences of the United States of America 107, 2010, pp. 7225–7229 (acccessed 2023/12/07/).JSTOR.
[51] A.K. Vannucci, L. Alibabaei, M.D. Losego, J.J. Concepcion, B. Kalanyan, G. N. Parsons, T.J. Meyer, Crossing the divide between homogeneous and heterogeneous catalysis in water oxidation, Proc. Natl. Acad. Sci. 110 (2013) 20918–20922.
[52] A. Bergmann, I. Zaharieva, H. Dau, P. Strasser, Electrochemical water splitting by layered and 3D cross-linked manganese oxides: correlating structural motifs and catalytic activity, Energy Environ. Sci. 6 (9) (2013) 2745–2755, https://doi.org/10.1039/C3EE41194J.
[53] T. Shinagawa, M.T.-K. Ng, K Takanabe, Electrolyte engineering towards efficient water splitting at mild pH, ChemSusChem. 10 (21) (2017) 4155–4162, https://doi.org/10.1002/cssc.201701266.
[54] T. Naito, T. Shinagawa, T. Nishimoto, K. Takanabe, Water electrolysis in saturated phosphate buffer at neutral pH, ChemSusChem. 13 (22) (2020) 5921–5933, https://doi.org/10.1002/cssc.202001886.
[55] T. Nishimoto, T. Shinagawa, T. Naito, K. Takanabe, Delivering the full potential of oxygen evolving electrocatalyst by conditioning electrolytes at near-neutral pH, ChemSusChem. 14 (6) (2021) 1554–1564, https://doi.org/10.1002/cssc.202002813.
[56] D.-Y. Kuo, J.K. Kawasaki, J.N. Nelson, J. Kloppenburg, G. Hautier, K.M. Shen, D. G. Schlom, J. Suntivich, Influence of surface adsorption on the oxygen evolution reaction on IrO2(110), J. Am. Chem. Soc. 139 (9) (2017) 3473–3479, https://doi.org/10.1021/jacs.6b11932.
[57] H. Dau, C. Pasquini, Modelling the (Essential) role of proton transport by electrolyte bases for electrochemical water oxidation at near-neutral pH, Inorganics 7 (2) (2019) 20.
[58] H. Ooka, A. Yamaguchi, T. Takashima, K. Hashimoto, R. Nakamura, Efficiency of oxygen evolution on iridium oxide determined from the pH dependence of charge accumulation, J. Phys. Chem. C 121 (33) (2017) 17873–17881, https://doi.org/10.1021/acs.jpcc.7b03749.
[59] Z. Li, Y. Wang, Y. Mu, B. Wu, Y. Jiang, L. Zeng, T. Zhao, Recent advances in the anode catalyst layer for proton exchange membrane fuel cells, Renew. Sustain. Energy Rev. 176 (2023) 113182, https://doi.org/10.1016/j.rser.2023.113182.
[60] S.D. Tilley, M. Cornuz, K. Sivula, M. Grätzel, Light-Induced water splitting with hematite: improved nanostructure and iridium oxide catalysis, Angew. Chem. Int. Ed. 49 (36) (2010) 6405–6408, https://doi.org/10.1002/anie.201003110.
[61] K.J. Jenewein, Y. Wang, T. Liu, T. McDonald, M. Zlatar, N. Kulyk, V. Benavente Llorente, A. Kormányos, D. Wang, S. Cherevko, Electrolyte engineering stabilizes photoanodes decorated with molecular catalysts, ChemSusChem. 16 (7) (2023) e202202319, https://doi.org/10.1002/cssc.202202319.
[62] W. Li, D. He, S.W. Sheehan, Y. He, J.E. Thorne, X. Yao, G.W. Brudvig, D. Wang, Comparison of heterogenized molecular and heterogeneous oxide catalysts for

photoelectrochemical water oxidation, Energy Environ. Sci. 9 (5) (2016) 1794–1802, https://doi.org/10.1039/C5EE03871E.
[63] W. Li, S.W. Sheehan, D. He, Y. He, X. Yao, R.L. Grimm, G.W. Brudvig, D. Wang, Hematite-Based solar water splitting in acidic solutions: functionalization by Mono- and Multilayers of iridium oxygen-evolution catalysts, Angew. Chem. Int. Ed. 54 (39) (2015) 11428–11432, https://doi.org/10.1002/anie.201504427.
[64] K.J. Jenewein, J. Knöppel, A. Hofer, A. Kormányos, B. Mayerhöfer, F.D. Speck, M. Bierling, S. Thiele, J. Bachmann, S. Cherevko, Dissolution of WO3 modified with IrOx overlayers during photoelectrochemical water splitting, SusMat 3 (1) (2023) 128–136, https://doi.org/10.1002/sus2.107.
[65] Y. Wang, D.Y.C. Leung, J. Xuan, H. Wang, A review on unitized regenerative fuel cell technologies, part-A: unitized regenerative proton exchange membrane fuel cells, Renew. Sustain. Energy Rev. 65 (2016) 961–977, https://doi.org/10.1016/j.rser.2016.07.046.
[66] G.C. da Silva, K.J.J. Mayrhofer, E.A. Ticianelli, S. Cherevko, The degradation of pt/irox oxygen bifunctional catalysts, Electrochim. Acta 308 (2019) 400–409, https://doi.org/10.1016/j.electacta.2019.04.017.
[67] G.C. da Silva, K.J.J. Mayrhofer, E.A. Ticianelli, S. Cherevko, Dissolution stability: the major challenge in the regenerative fuel cells bifunctional catalysis, J. Electrochem. Soc. 165 (16) (2018) F1376, https://doi.org/10.1149/2.1201816jes.
[68] C.-Q. Yi, J.-P. Zou, H.-Z. Yang, X. Leng, Recent advances in pseudocapacitor electrode materials: transition metal oxides and nitrides, Trans. Nonferrous Metals Soc. China 28 (10) (2018) 1980–2001, https://doi.org/10.1016/S1003-6326(18)64843-5.
[69] S. Chandrabose Raghu, M. Ulaganathan, T.M. Lim, M. Skyllas Kazacos, Electrochemical behaviour of titanium/iridium(IV) oxide: tantalum pentoxide and graphite for application in vanadium redox flow battery, J. Power Sources 238 (2013) 103–108, https://doi.org/10.1016/j.jpowsour.2013.03.084.
[70] E. McCalla, A.M. Abakumov, M. Saubanère, D. Foix, E.J. Berg, G. Rousse, M.-L. Doublet, D. Gonbeau, P. Novák, G. Van Tendeloo, R. Dominko, J.-M. Tarascon, Visualization of O-O peroxo-like dimers in high-capacity layered oxides for Li-ion batteries, Science 350 (6267) (2015) 1516–1521, https://doi.org/10.1126/science.aac8260.
[71] E. Slavcheva, R. Vitushinsky, W. Mokwa, U. Schnakenberg, Sputtered iridium oxide films as charge injection material for functional electrostimulation, J. Electrochem. Soc. 151 (7) (2004) E226, https://doi.org/10.1149/1.1747881.
[72] M. Zea, A. Moya, M. Fritsch, E. Ramon, R. Villa, G. Gabriel, Enhanced performance stability of iridium oxide-based pH sensors fabricated on rough inkjet-printed platinum, ACS Appl. Mater. Interfaces 11 (16) (2019) 15160–15169, https://doi.org/10.1021/acsami.9b03085.
[73] Y. Chen, X. Li, D. Li, C. Batchelor-McAuley, R.G. Compton, A simplified methodology: pH sensing using an in situ fabricated ir electrode under neutral conditions, J. Solid State Electrochem. 25 (12) (2021) 2821–2833, https://doi.org/10.1007/s10008-021-05017-6.
[74] W. Olthuis, M.A.M. Robben, P. Bergveld, M. Bos, W.E. van der Linden, pH sensor properties of electrochemically grown iridium oxide, Sens. Actuators B 2 (4) (1990) 247–256, https://doi.org/10.1016/0925-4005(90)80150-X.
[75] L.D. Burke, J.K. Mulcahy, D.P. Whelan, Preparation of an oxidized iridium electrode and the variation of its potential with pH, J. Electroanal. Chem. Interfac. Electrochem. 163 (1) (1984) 117–128, https://doi.org/10.1016/S0022-0728(84)80045-5.
[76] J. Backholm, G.A. Niklasson, Optical properties of electrochromic iridium oxide and iridium–tantalum oxide thin films in different colouration states, Sol. Energy Mater. Sol. Cells 92 (11) (2008) 1388–1392, https://doi.org/10.1016/j.solmat.2008.05.015.
[77] H. Yang, S.K. Kang, C.A. Choi, H. Kim, D.-H. Shin, Y.S. Kim, Y.T. Kim, An iridium oxide reference electrode for use in microfabricated biosensors and biochips, Lab Chip 4 (1) (2004) 42–46, https://doi.org/10.1039/B309899K.
[78] Q. Dong, X. Sun, S. He, Iridium oxide enabled sensors applications, Catalysts. 11 (10) (2021) 1164.
[79] C. Ma, P. Fang, Z.-R. Liu, S.-S. Xu, K. Xu, X. Cheng, A. Lei, H.-C. Xu, C. Zeng, T.-S. Mei, Recent advances in organic electrosynthesis employing transition metal complexes as electrocatalysts, Sci. Bull. 66 (23) (2021) 2412–2429, https://doi.org/10.1016/j.scib.2021.07.011.
[80] A. Weiß, A. Siebel, M. Bernt, T.H. Shen, V. Tileli, H.A. Gasteiger, Impact of intermittent operation on lifetime and performance of a PEM water electrolyzer, J. Electrochem. Soc. 166 (8) (2019) F487, https://doi.org/10.1149/2.0421908jes.
[81] Stojanovski, K.; Briega-Martos, V.; Zlatar, M.; Göllner, C.; Cherevko, S. pH Dependence of Noble Metals Dissolution: Gold. *ChemElectroChem n/a* (n/a), e202400373. DOI: https://doi.org/10.1002/celc.202400373.
[82] V. Briega-Martos, K. Stojanovski, M. Zlatar, C. Göllner, S. Cherevko, pH dependence of noble metals dissolution: platinum, Electrochim. Acta (2024) 144793, https://doi.org/10.1016/j.electacta.2024.144793.
[83] S.O. Klemm, A.A. Topalov, C.A. Laska, K.J.J. Mayrhofer, Coupling of a high throughput microelectrochemical cell with online multielemental trace analysis by icp-ms, Electrochem. Commun. 13 (12) (2011) 1533–1535, https://doi.org/10.1016/j.elecom.2011.10.017.
[84] M. Zlatar, D. Escalera-López, M.G. Rodríguez, T. Hrbek, C. Götz, R. Mary Joy, A. Savan, H.P. Tran, H.N. Nong, P. Pobedinskas, V. Briega-Martos, A. Hutzler, T. Böhm, K. Haenen, A. Ludwig, I. Khalakhan, P. Strasser, S Cherevko, Standardizing OER electrocatalyst benchmarking in aqueous electrolytes: comprehensive guidelines for accelerated stress tests and backing electrodes, ACS Catal. 13 (23) (2023) 15375–15392, https://doi.org/10.1021/acscatal.3c03880.
[85] J. Mozota, B.E. Conway, Surface and bulk processes at oxidized iridium electrodes—I. Monolayer stage and transition to reversible multilayer oxide film behaviour, Electrochim. Acta 28 (1) (1983) 1–8, https://doi.org/10.1016/0013-4686(83)85079-8.
[86] B.E. Conway, J. Mozota, Surface and bulk processes at oxidized iridium electrodes—II. Conductivity-switched behaviour of thick oxide films, Electrochim. Acta 28 (1) (1983) 9–16, https://doi.org/10.1016/0013-4686(83)85080-4.
[87] L.D. Burke, D.P. Whelan, A voltammetric investigation of the charge storage reactions of hydrous iridium oxide layers, J. Electroanal. Chem. Interfac. Electrochem. 162 (1) (1984) 121–141, https://doi.org/10.1016/S0022-0728(84)80159-X.
[88] C. Bock, V.I. Birss, Anion and water involvement in hydrous Ir oxide redox reactions in acidic solutions, J. Electroanal. Chem. 475 (1) (1999) 20–27, https://doi.org/10.1016/S0022-0728(99)00330-7.
[89] X. Tan, J. Shen, N. Semagina, M. Secanell, Decoupling structure-sensitive deactivation mechanisms of Ir/IrOx electrocatalysts toward oxygen evolution reaction, J. Catal. 371 (2019) 57–70, https://doi.org/10.1016/j.jcat.2019.01.018.
[90] T. Reier, M. Oezaslan, P. Strasser, Electrocatalytic oxygen evolution reaction (OER) on Ru, Ir, and Pt catalysts: a comparative study of nanoparticles and bulk materials, ACS Catal. 2 (8) (2012) 1765–1772, https://doi.org/10.1021/cs3003098.
[91] M. Pourbaix, Atlas of Electrochemical Equilibria in Aqueous Solutions, National Association of Corrosion Engineers, 1974.
[92] S. Cherevko, Electrochemical dissolution of noble metals, in: K. Wandelt (Ed.), Encyclopedia of Interfacial Chemistry, Elsevier, 2018, pp. 68–75.
[93] O. Kasian, J.-P. Grote, S. Geiger, S. Cherevko, K.J.J. Mayrhofer, The common intermediates of oxygen evolution and dissolution reactions during water electrolysis on iridium, Angew. Chem. Int. Ed. 57 (9) (2018) 2488–2491, https://doi.org/10.1002/anie.201709652.
[94] M. Hüppauff, B. Lengeler, Valency and structure of iridium in anodic iridium oxide films, J. Electrochem. Soc. 140 (3) (1993) 598, https://doi.org/10.1149/1.2056127.
[95] S. Cherevko, Electrochemical dissolution of noble metals native oxides, J. Electroanal. Chem. 787 (2017) 11–13, https://doi.org/10.1016/j.jelechem.2017.01.029.
[96] M. Zlatar, D. Nater, D. Escalera-López, R.M. Joy, P. Pobedinskas, K. Haenen, C. Copéret, S. Cherevko, Evaluating the stability of Ir single atom and Ru atomic cluster oxygen evolution reaction electrocatalysts, Electrochim. Acta 444 (2023) 141982, https://doi.org/10.1016/j.electacta.2023.141982.
[97] K.J. Vetter, J.W. Schultze, The kinetics of the electrochemical formation and reduction of monomolecular oxide layers on platinum in 0.5 M H2SO4: part II. Galvanostatic pulse measurements and the model of oxide growth, J. Electroanal. Chem. Interfac. Electrochem. 34 (1) (1972) 141–158, https://doi.org/10.1016/S0022-0728(72)80510-2.
[98] B.E. Conway, Electrochemical oxide film formation at noble metals as a surface-chemical process, Prog. Surf. Sci. 49 (4) (1995) 331–452, https://doi.org/10.1016/0079-6816(95)00040-6.
[99] S. Cherevko, A.R. Zeradjanin, G.P. Keeley, K.J.J. Mayrhofer, A comparative study on gold and platinum dissolution in acidic and alkaline media, J. Electrochem. Soc. 161 (12) (2014) H822–H830, https://doi.org/10.1149/2.0881412jes.
[100] S. Cherevko, A.A. Topalov, A.R. Zeradjanin, I. Katsounaros, K.J.J. Mayrhofer, Gold dissolution: towards understanding of noble metal corrosion, RSC Adv. 3 (37) (2013) 16516–16527, https://doi.org/10.1039/C3RA42684J.
[101] A.A. Topalov, S. Cherevko, A.R. Zeradjanin, J.C. Meier, I. Katsounaros, K.J. J. Mayrhofer, Towards a comprehensive understanding of platinum dissolution in acidic media, Chem. Sci. 5 (2) (2014) 631–638. Article. DOI: 10.1039/c3sc52411f Scopus.
[102] A.A. Topalov, A.R. Zeradjanin, S. Cherevko, K.J.J. Mayrhofer, The impact of dissolved reactive gases on platinum dissolution in acidic media, Electrochem. Commun. 40 (2014) 49–53, https://doi.org/10.1016/j.elecom.2013.12.021.
[103] A. Ganassin, V. Colic, J. Tymoczko, A.S. Bandarenka, W. Schuhmann, Non-covalent interactions in water electrolysis: influence on the activity of Pt(111) and iridium oxide catalysts in acidic media, Phys. Chem. Chem. Phys. 17 (13) (2015) 8349–8355, https://doi.org/10.1039/C4CP04791E.
[104] B.E. Conway, B. Barnett, H. Angerstein-Kozlowska, B.V. Tilak, A surface-electrochemical basis for the direct logarithmic growth law for initial stages of extension of anodic oxide films formed at noble metals, J. Chem. Phys. 93 (11) (1990) 8361–8373, https://doi.org/10.1063/1.459319. Article. DOIScopus.
[105] M.W. Breiter, Mechanism of the formation and reduction of the oxygen layer on iridium in sulphuric acid solution, Zeitschrift für Physikalische Chemie 52 (1_4) (1967) 73–88, https://doi.org/10.1524/zpch.1967.52.1_4.073 *(acccessed 2024-11-18)*.
[106] T. Fuchs, V. Briega-Martos, J. Drnec, N. Stubb, I. Martens, F. Calle-Vallejo, D. A. Harrington, S. Cherevko, O.M. Magnussen, Anodic and cathodic platinum dissolution processes involve different oxide species, Angew. Chem. Int. Ed. 62 (34) (2023) e202304293, https://doi.org/10.1002/anie.202304293.
[107] M.W. Kanan, D.G. Nocera, In situ formation of an oxygen-evolving catalyst in neutral water containing phosphate and Co^{2+}, Science 321 (5892) (2008) 1072–1075, https://doi.org/10.1126/science.1162018.
[108] Y. Surendranath, M.W. Kanan, D.G. Nocera, Mechanistic studies of the oxygen evolution reaction by a cobalt-phosphate catalyst at neutral pH, J. Am. Chem. Soc. 132 (46) (2010) 16501–16509, https://doi.org/10.1021/ja106102b.

[109] D.A. Lutterman, Y. Surendranath, D.G. Nocera, A self-healing oxygen-evolving catalyst, J. Am. Chem. Soc. 131 (11) (2009) 3838–3839, https://doi.org/10.1021/ja900023k.
[110] R. Zhang, N. Dubouis, M. Ben Osman, W. Yin, M.T. Sougrati, D.A.D. Corte, D. Giaume, A. Grimaud, A dissolution/precipitation equilibrium on the surface of iridium-based perovskites controls their activity as oxygen evolution reaction catalysts in acidic media, Angew. Chem. Int. Ed. 58 (14) (2019) 4571–4575, https://doi.org/10.1002/anie.201814075.
[111] R. Kötz, H. Neff, S. Stucki, Anodic iridium oxide films: xPS-Studies of oxidation state changes and, J. Electrochem. Soc. 131 (1) (1984) 72, https://doi.org/10.1149/1.2115548.